Climate Dynamics (2024) 62:2057–2067
https://doi.org/10.1007/s00382-023-07010-3

ORIGINAL ARTICLE

The sensitivity of climate and climate change to the efficiency of atmospheric heat transport

Qi Ge[1] · Zhihua Zheng[2] · Litai Kang[1] · Aaron Donohoe[1,3] · Kyle Armour[1,2] · Gerard Roe[4]

Received: 25 July 2023 / Accepted: 30 October 2023 / Published online: 7 December 2023
© The Author(s), under exclusive licence to Springer-Verlag GmbH Germany, part of Springer Nature 2023

Abstract

Atmospheric heat transport (AHT) moderates spatial gradients in surface temperature, and its efficiency (hereinafter referred to as diffusivity) shapes the distribution of moist static energy and the hydrological cycle. Using a linear downgradient rule for AHT, we diagnose zonal-mean diffusivity using observational and model data. We find it varies two- to threefold with season and latitude, but is nearly invariant across different climate states. We then employ a moist energy balance model (MEBM) to explore the impacts of changing the magnitude and spatial pattern of diffusivity on the climatology and climate response to forcing. Spatial anomalies in diffusivity in the extra-tropics have a larger impact on temperature and hydrology than diffusivity anomalies in the tropics. We demonstrate that compensating dynamical adjustments in the MEBM act to mute the impact of changing diffusivity patterns on the resulting climate. We isolate the impacts of spatial patterns of forcing, ocean heat uptake, radiative feedbacks, and diffusivity on the spatial pattern of climate change; and find that the pattern of climate change is least sensitive to the detailed pattern of diffusivity. Overall, these results suggest that although diffusivity is far from spatially invariant, understanding the climatology and spatial patterns of climate change does not depend on a detailed characterization of the spatial pattern of diffusivity.

Keywords Atmospheric heat transport · Diffusivity · Energy balance model · Climate response · Hydrologic cycle

1 Introduction

Poleward atmospheric heat transport (AHT) moderates spatial gradients in Earth's temperature in both the climatological state and the response to external forcing. In the absence of AHT, the equator-to-pole temperature gradient mandated by local radiative equilibrium is approximately three times larger than that observed (Pierrehumbert 2010). In response to external forcing, changes in AHT generally move energy away from regions of strong forcing/less efficient radiative damping (Feldl and Roe 2013), thereby reducing the spatial gradients in temperature change implied by local radiative considerations alone. Changes in AHT reduce the global-mean temperature response to external forcing—climate sensitivity—by moving energy to regions where energy can efficiently be lost to space (Feldl and Roe 2013; Armour et al. 2019).

Poleward AHT and its response to external forcing is often approximated by the (linear) downgradient diffusion of moist static energy (MSE) at the surface, where surface MSE is defined as the sum of sensible and latent energy (Flannery1984; Hwang and Frierson 2010; Hwang et al. 2011; Rose et al. 2014; Roe et al. 2015; Merlis and Henry 2018; Armour et al. 2019; Merlis et al. 2022). Importantly, the temperature and AHT response to external forcing can be predicted reasonably well using a moist energy balance model (MEBM) with a spatially invariant diffusion coefficient (D) diagnosed from the climatological relationship between AHT and the MSE gradient. The atmospheric MSE diffusion framework with a spatially and climate-state invariant D has been successfully applied at scales ranging from inter-hemispheric to equator-to-pole, and in both comprehensive and idealized models (e.g., Hwang and Frierson

✉ Gerard Roe
groe@uw.edu

1 Department of Atmospheric Sciences, University of Washington, Seattle, WA 98195, USA

2 School of Oceanography, University of Washington, Seattle, WA 98195, USA

3 Polar Science Center, Applied Physics Laboratory, University of Washington, Seattle, WA 98105, USA

4 Department of Earth and Space Sciences, University of Washington, Seattle, WA 98195, USA

2010; Hwang et al. 2011; Rose et al. 2014; Armour et al. 2019; Cox et al. 2022).

The success of MEBMs with spatially and climate-state invariant D in quantitatively describing the climate system behavior is surprising because the mechanisms underlying AHT are neither spatially nor climate-state invariant. Although the total AHT varies smoothly from equator-to-pole (Trenberth and Caron 2001), the atmospheric motions that accomplish AHT differ substantially between: (i) the deep tropics, where lateral temperature gradients are weak and poleward AHT is achieved by the time-mean mass-overturning circulation of the Hadley cells (with poleward flow aloft and equatorward flow at the surface), which moves energy by virtue of the increasing MSE with height in the atmosphere; and (ii) the mid-latitudes, where the meridional temperature gradient is strong and poleward AHT is achieved primarily by fluctuations in MSE and winds (e.g., transient eddies) in which times of poleward flow are relatively warm and wet and times of equatorward flow are relatively cold and dry, on average. While the MSE diffusion framework offers a plausible improvement on the diffusion-of-temperature framework (e.g., North 1975) for bridging tropical and midlatitude regimes with a spatially invariant D, an emerging body of work demonstrates that D diagnosed from the ratio of AHT and MSE gradients is neither spatially invariant (Mooring and Shaw 2020) nor climate-state invariant (Shaw and Voigt 2016). The existing theories for what determines D (e.g., Barry 2002; Lapeyre and Held 2004; Chang et al. 2022) are generally based on turbulence theory, most apt for describing baroclinic-eddy lifecycles; and it is unclear if these theories can be generalized to include atmospheric heat transport by the Hadley cell or mechanically forced stationary eddies (Cox et al. 2022) which likely induce spatially varying modifications to the efficiency of AHT. A global theory for D and its changes (or invariance) under global warming must relate changes in the vertical gradient of MSE in the tropics (e.g., gross moist stability) to the changes in horizontal gradients of surface MSE. We know of no literature that provides a basis for time and spatially invariant D, whereas there are a multitude of dynamic and thermodynamic reasons D should vary in space and time.

In this work, we attempt to reconcile the general success of MEBMs with spatially and temporally invariant D with the emerging understanding that D varies in space and time. The overarching question is: are spatial–temporal variations in D large enough to have a climate impact (relative to the climate system with uniform and constant D)? The following sequential approach is taken: we evaluate how much D varies in space and time and then ask how much these variations in D impact climate. Specifically, we begin by diagnosing the spatial and seasonal variations in D using observational data and climate models, and analyze how D changes in models with climate states (Sect. 2). We then ask how much the diagnosed spatial/temporal variations in D impact climate by comparing: (i) the MEBM prediction using spatially/temporally varying D versus (ii) the MEBM prediction using a uniform and constant D. The climate impact of spatial/temporal variations in D is analyzed for both the mean-state climate (Sect. 3) and forced perturbations (Sect. 4). We finish by analyzing the degree to which spatial/temporal variations in D impact climate change as compared to the climate impact of spatial variations in radiative forcing, radiative feedbacks and ocean heat uptake (Sect. 5).

Our primary focus is on the MEBM's ability to predict surface temperature and AHT. The moist component of AHT is also closely tied to the hydrological cycle (Siler et al. 2018; Bonan et al. 2023): the divergence of latent heat transport (divided by latent heat of vaporization) is equal to evaporation minus precipitation ($E - P$). In the tropics a parameterization of the Hadley Cell transport is incorporated into the overall diffusive downgradient AHT transport (Siler et al. 2018, see also Appendix A), allowing for latent-heat fluxes to be diagnosed. This hydrological extension of the MEBM allows the impact of spatial/temporal variations in D on the hydrological cycle to be analyzed. We analyze the temperature and hydrological sensitivity in concert throughout this manuscript.

2 Diagnosing diffusivity in reanalyses and GCMs

We begin by diagnosing the meridional pattern of diffusivity using modern-day reanalysis and general-circulation-model (GCM) simulations of the pre-industrial climate, a world with CO_2 four times higher ($4 \times CO_2$), and the Last Glacial Maximum (LGM). Let $x = \sin(\theta)$, where θ is latitude. The zonally and vertically integrated AHT, $F(x)$, is related to the near-surface MSE ($\equiv h$) gradient via:

$$F(x) = -2\pi \frac{p_s}{g} \bullet D(x) \bullet (1 - x^2) \frac{dh}{dx} \tag{1}$$

where p_s/g is surface air pressure divided by gravitational acceleration giving the mass of the column per unit area; $D(x)$ is the latitudinally varying zonal-mean diffusivity (in units of $m^2\ s^{-1}$); and $h = c_p T + Lq$, where c_p is the specific heat of air,T is near-surface (2 m) air temperature, L is the latent heat of vaporization, and q is near-surface specific humidity. The factor $(1 - x^2)$ accounts for spherical geometry in relating the zonally integrated $F(x)$ (in units of PW) to the MSE gradient. Equation (1) can be rearranged to solve for diffusivity:

$$D(x) = -\frac{g}{p_s} \bullet \frac{1}{2\pi} \bullet \frac{1}{(1-x^2)} \bullet \left(\frac{dh}{dx}\right)^{-1} F(x) \quad (2)$$

We calculate observed $F(x)$ from ERA5 reanalysis (Hersbach et al. 2020) following Donohoe et al. (2020) as the monthly average of the vertical- and zonal-integrated product of MSE and meridional velocity after a mass flux correction. We evaluate the near-surface MSE (h) using T calculated from the zonal mean of ERA5 and assuming a fixed relative humidity of 0.8, for simplicity. In order to reduce noise, we calculate an average D in 15° latitude bins using least-squares regression outside of 15° N to 15° S. However, within the deep tropics there are regions where the MSE gradients are near zero, and here we use L'Hôpital's rule to resolve the singularity issue using a non-zero-intercept linear fit within 15°N to 15°S. The dots in Fig. 1 show the results for each bin. Finally, we use fourth-order Legendre-polynomial fit to interpolate over all latitudes (the curves in Fig. 1). We found this approach strikes an appropriate balance between simplicity and realism. Our results for $D(x)$ were similar for latitude bins varying from 10° to 20°, and for third- to fifth-order smoothing.

Figure 1a shows $D(x)$ diagnosed from ERA5 reanalyses (averaged over 2000 to 2020). Values of $D(x)$ for the annual mean ($\equiv D_{obs}$), for December-February (DJF), and June–August (JJA) all show two- to three-fold spatial variations. All curves show D peaking in the mid-latitudes, with lower values in the tropics and high latitudes, consistent with higher values of D in the vicinity of the storm track (e.g., Shaw and Voigt 2016). We also compare D_{obs} to the spatially-uniform, annual-mean value $\overline{D} = 1.05 \times 10^6 \mathrm{m^2 s^{-1}}$ that produces a meridional temperature structure with the best match to ERA5 when using the MEBM (Sect. 3.2), following previous studies. Note that the best-fit constant $\overline{D}$ is most similar to the mid-latitude values of $D_{obs}(x)$, reflecting the greater importance of the value of diffusivity where the gradients of h are larger. Note also that our value of $\overline{D}$ is within 10% of the value used in previous studies: $0.96 \times 10^6 \mathrm{m^2 s^{-1}}$ in Armour et al. (2019), $1.16 \times 10^6 \mathrm{m^2 s^{-1}}$ in Siler et al. (2018), and $1.06 \times 10^6 \mathrm{m^2 s^{-1}}$ in Hwang and Frierson (2010). Shaw and Voigt (2016) diagnosed $D(x)$ in an ensemble of aquaplanet-configured GCMs, and found a similar (albeit amplified) spatial structure. At most latitudes, there is an approximately two-fold seasonal cycle in D, maximizing in the winter mid-latitudes.

Figure 1b shows $D(x)$ diagnosed using the same procedure (Eq. (2)) for three other climate states using the ensemble-mean averages of ten GCMs participating in phase 5 of the Coupled Model Intercomparison Project (CMIP5; Taylor et al. 2012) for the following simulations: pre-industrial (*piControl*); years 50–100 after an abrupt CO_2 quadrupling (abrupt $4 \times CO_2$; and the LGM (as part of the Paleoclimate Model Intercomparison Project, PMIP3; Braconnot et al. 2012). More details of the models analyzed are provided in Appendix Table 1. We find that $D(x)$ is remarkably similar across these three widely differing climate states, although there is a slight indication that D_{4x} increases in high northern latitudes under CO_2 quadrupling. We note the spatial pattern of $D(x)$ diagnosed in the CMIP5 models is amplified in the mid-latitudes compared to that in reanalysis.

These results suggest that diffusivity varies in both space (factor of three) and seasonally (factor of two at a given location) but that diffusivity is relatively invariant to climate state in coupled model simulations.

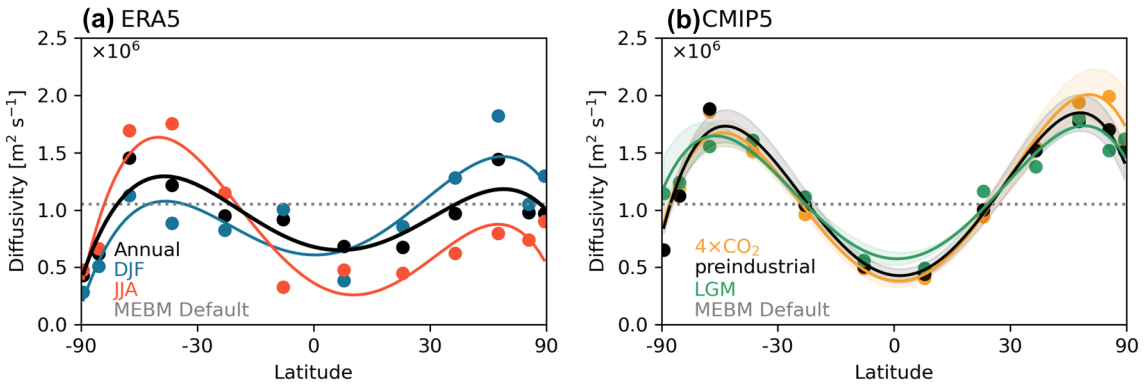

Fig. 1 The diagnosed diffusivity, $D(x)$ from (**a**) ERA5 reanalysis for the annual mean (black), DJF (blue), and JJA (red); and (**b**) CMIP5 simulations in three different climate states: pre-industrial (black), $4\times CO_2$ (yellow), and LGM (green). In both panels, dots represent diagnosed mean D in each 15° latitude, and lines show a 4th-order Legendre-polynomial fit. In the panel (**a**), the grey dashed line shows $D = 1.05 \times 10^6 \mathrm{m^2 s^{-1}}$ that produces a meridional temperature pattern in the climatological MEBM (Sect. 3.2) with the best match with ERA5. In the panel (**b**), the shading represents one standard deviation from the mean D of each climate state for full spread of models. The grey dashed line shows $D = 1.05 \times 10^6 \mathrm{m^2 s^{-1}}$. Note that the x-axes are area-weighted so that they are linear in $x = \sin(\theta)$, where θ is latitude (same for all figures below)

2.1 The impact of diffusivity on the mean-state climatology

In this Section, we examine the sensitivity of the mean-state climatology to changes in diffusivity using two approaches. First, we prescribe AHT as derived from ERA5, allowing only $T(x)$ to adjust to varying patterns of $D(x)$ in Eq. (1) (Sect. 3.1). Second, we explore the climate response to varying patterns of $D(x)$ within the framework of MEBM where temperature and AHT can adjust simultaneously (Sect. 3.2).

2.2 Climate solutions using the observed atmospheric heat transport

We first evaluate the impact of spatially-varying $D(x)$ on the climatology by imposing the observed AHT, $F(x)$, on the left-hand side of Eq. (1) and solving for the required spatial structure of h for a given $D(x)$. Because h is a single-valued function of T (assuming fixed relative humidity) we can find the required spatial pattern of T, with the additional constraint that the global-mean temperature matches the observations.

We use either $\overline{D}$ or $D_{obs}(x)$ (shown in Fig. 2a) on the right-hand side of Eq. (2), and calculate the resulting $T(x)$. Note that, because of the fitting and smoothing, using $D_{obs}(x)$ will not exactly reproduce the observed $T(x)$. Figure 2b shows that using the constant-valued $\overline{D}$ produces slight mismatches in the temperature gradients at high latitudes, compared to using $D_{obs}(x)$. The somewhat larger values of $D_{obs}(x)$, compared to $\overline{D}$, in the midlatitudes require less-steep temperature gradients to achieve the prescribed AHT. However, using constant $\overline{D}$ still closely predicts the observed temperature profile, with a root-mean-square error of 1.5 °C. Changes in $T(x)$ are small for two reasons. First, it is changes in dh/dx that balance changes in $D(x)$ (Eq. 1) and, because of moisture, changes in dT/dx are smaller than dh/dx. Second, since $T(x)$ is the integral of dT/dx, its pattern of adjustment is smoother.

Siler et al. (2018) extended the downgradient AHT parameterization to enable a calculation of the latent heat fluxes and hence $E-P$. In the extratropics, the sensible heat (c_pT) and latent heat (Lq) components are diffused with the same diffusivity according to Eq. (1). However, in the tropics, while total heat transport is governed by Eq. (1), latent-heat fluxes are diagnosed from the overall downgradient transport of MSE using a Hadley-Cell parameterization following Held (2001), outlined here in Appendix A. The transition between the tropical and extratropical regimes occurs via a latitudinally varying weighting function (Siler et al. 2018; Armour et al. 2019; Bonan et al. 2018, 2023; and Appendix A).

Consistent with Siler et al. (2018), when we use $D_{obs}(x)$ and the observed AHT as input, our hydrologic scheme gives good agreement to observed $E-P$ (cf. the red and grey lines in Fig. 2c). Switching diffusivity input from $D_{obs}(x)$ to a spatially invariant $\overline{D}$ has minimal impact on the resulting pattern of $E-P$(cf. the red and black lines in Fig. 2c). We interpret the weak sensitivity of the hydrological cycle to spatial patterns of D (under fixed AHT) as follows: since total AHT is constrained in this Section and the ratio of moist to dry AHT is a function primarily

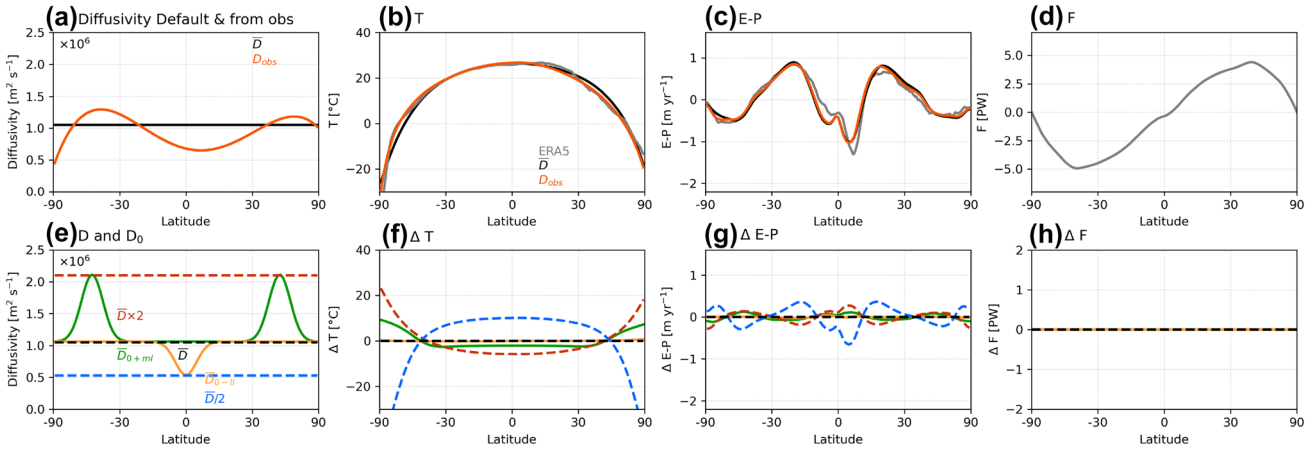

Fig. 2 Effects of different patterns of diffusivity, $D(x)$, on the climatology for fixed AHT. First row evaluates the impact of spatially-varying versus spatially-uniform diffusivity: (**a**) diffusivity patterns diagnosed from observation (red) and spatially-uniform diffusivity (black) that gives best-fit to observations; (**b**) T and (**c**) E-P calculated using Eq. (1) with these two diffusivity patterns, and corresponding observations (grey lines); and (**d**) the observed AHT prescribed in Eq. (1). Second row evaluates the impact of varying the magnitude or pattern of diffusivity: (**e**) synthetic patterns of $D(x)$; (**f**), (**g**), and (**h**) are as for top row, but show differences from the spatially-uniform solutions. All observations are from ERA5. The global mean of $T(x)$ calculated from Eq. (1) has been set equal to the mean of the observations in both rows

of extratropical/tropical regime and only weakly of local thermodynamics (Clausius Clapeyron and atmospheric stability), the modest changes in temperature with spatial patterns of diffusivity have only a small impact on moisture fluxes.

The second row of Fig. 2 again uses the observed AHT on the left-hand side of Eq. (1), but we now evaluate the impact of varying the magnitude or pattern of diffusivity with various synthetic patterns shown in Fig. 2e. The synthetic patterns of diffusivity are generated based on the seasonal and spatial variations seen in Fig. 1a. Because the AHT is fixed, change in $D(x)$ must be balanced by changes in dh/dx, and hence $T(x)$.

First, we create two diffusivity patterns, one with a negative anomaly in tropics (yellow line in Fig. 2e) and the other a positive anomaly in midlatitudes (green line in Fig. 2e), inspired by observed diffusivity pattern in Fig. 1a. A negative anomaly applied in the deep tropics has very little impact on T (with $\Delta T < 1$ °C everywhere) and $E-P$. With fixed AHT, gradients of dh/dx (and dT/dx) are small in the tropics, and so changing D there has little impact. Furthermore, for a given temperature change in the tropics, near-surface MSE is approximately three-parts moisture (Lq) to one-part dry energy (c_pT), the adjustments in MSE gradient needed to conserve AHT under altered D can be satisfied with small temperature changes. A positive anomaly in $D(x)$ in the mid-latitudes has a larger impact on $T(x)$ (Fig. 2f), drawing heat out of the tropics (cooling the tropics by ~ 2 °C); and the resulting heat transport warms the high latitudes by ~ 5 °C. As we saw before, this shows that midlatitude anomalies in D have a bigger impact than tropical anomalies.

We also use spatially-uniform diffusivities of different magnitudes to examine the changes in resulting T and $E-P$. Setting $D(x)=\overline{D}/2$ requires a doubling of dh/dx in order to maintain the same AHT, resulting in large changes in h and thus producing strong tropical warming (> 10 °C) and high-latitude cooling (> 20 °C) (blue dashed line in Fig. 2f). The increased moisture gradients amplify the hydrologic cycle (Fig. 2g). Taking $D(x)=2\times\overline{D}$ requires a halving of dh/dx; and so the magnitude of the changes in $h(x)$, and hence $T(x)$, are less than for the $D(x)=\overline{D}/2$ case. Similarly, changing $D(x)$ everywhere imposes larger changes in h than changing $D(x)$ locally.

2.3 Climate solutions using a moist energy balance model

We next evaluate the impact of spatial patterns in $D(x)$ on the spatial patterns of T and $E-P$ in the framework of a moist energy balance model (MEBM). The MEBM satisfies the zonal-mean energy balance which, assuming no ocean heat transport, requires a balance between net radiation at the top of the atmosphere and atmospheric heat transport (F) divergence:

$$ASR-\underbrace{(A+BT)}_{OLR}=\underbrace{\frac{p_S}{ga^2}\frac{d}{dx}\left[D(x)\left(1-x^2\right)\frac{dh}{dx}\right]}_{\nabla\cdot F(x)} \tag{3}$$

The first term is the absorbed solar radiation (ASR) at the top-of-the-atmosphere, which we take from ERA5 reanalysis. The second term is a linearization of the outgoing longwave radiation (OLR) in terms of temperature, and we set $A=205$ W m^{-2}, and $B=2.44$ W m^{-2} K^{-1}. These values of A and B provide a good fit to the climatological OLR and T. However, provided the parameters selected avoid the extreme limits of radiative-damping efficiency, our results assessing the importance of the spatial pattern of $D(x)$ hold. The right-hand side is the divergence of the AHT. Traditional, dry, versions of energy balance models (EBMs) assume a temperature-based transport rule, and so use T rather than h on the right-hand side (e.g., North 1975). In the dynamical system represented by Eq. (3), both the temperature and AHT can adjust to the prescribed patterns of diffusivity $D(x)$.

Using the full spatial structure of D_{obs} in the MEBM results in a climatological temperature that is very similar to that found using a spatially invariant D (cf. the black and red lines in Fig. 3b). Importantly, climatological temperature is less sensitive to spatial patterns in D in the full MEBM as compared to the sensitivity under fixed AHT (i.e., the red and black lines are closer together in Fig. 3b as compared to 2b).

The weaker sensitivity of temperature to spatial patterns in D when AHT can adjust (cf. fixed AHT) can be understood as follows. Consider the midlatitude Southern Ocean (near 50°S) where D_{obs} is larger than $\overline{D}$ (Fig. 3a); and consider initially having the equilibrium temperature solution with $D=\overline{D}$ (black line in Fig. 3b). When instantaneously subjecting it to $D=D_{obs}$, the enhanced diffusivity in this region will result in increased poleward AHT (before any temperature adjustment has taken place), which will weaken the temperature gradient. In the fixed AHT setting, the temperature gradient must reduce its slope (i.e., the red line in Fig. 2b) to the point the prescribed AHT is restored. In the full MEBM, the instantaneous enhancement of D when switching from $\overline{D}$ to D_{obs} also results in a surplus of AHT into the extratropical Southern Ocean (Fig. 3d) and a warming tendency in this region. As the regions poleward of the AHT maxima warm, two damping energetic tendencies counterbalance the energy surplus: (i) the temperature gradient shallows, thereby reducing the AHT anomaly caused by the diffusivity perturbation alone (under the temperature profile from $D=\overline{D}$) and; (ii) the increased temperature results in enhanced radiative energy loss via OLR (the

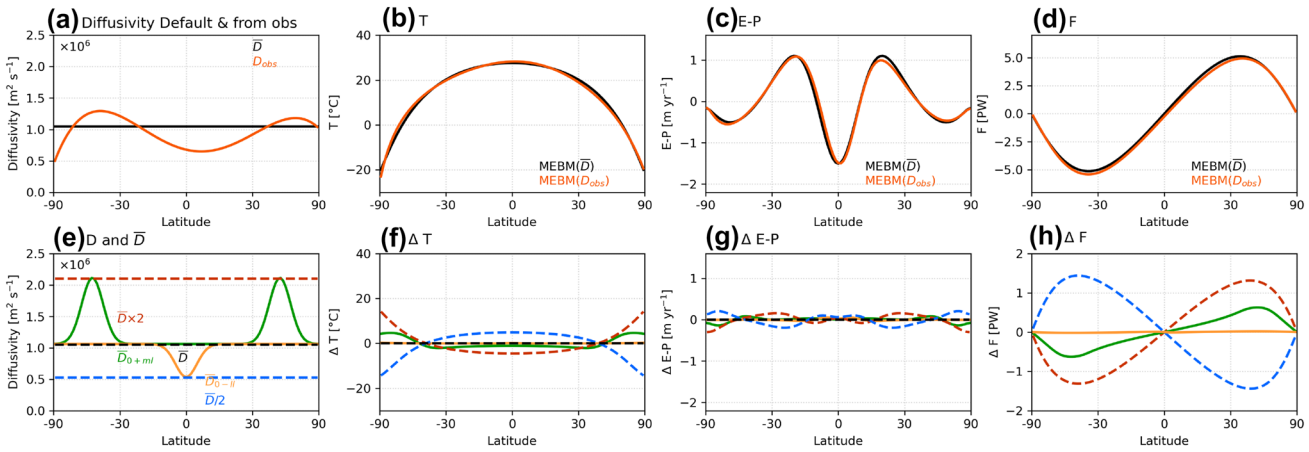

Fig. 3 As in Fig. 2, the effects of different patterns of diffusivity, $D(x)$, on the climatology, but for the MEBM rather than for fixed $F(x)$. First row evaluates the impact of spatially-varying versus spatially-uniform diffusivity: (**a**) diffusivity patterns diagnosed from observation (red) and spatially-uniform diffusivity (black) that gives best-fit to observations; (**b**) T, (**c**) E-P, and (**d**) $F(x)$ calculated using the MEBM (Eq. 3) with these two diffusivity patterns. Second row evaluates the impact of varying the magnitude or pattern of diffusivity: (**e**) synthetic patterns of $D(x)$; (**f**), (**g**), and (**h**) are as for top row, but show differences from the spatially-uniform solutions

Planck feedback). Thus, in the full MEBM the temperature adjustment to prescribed spatial anomalies in D is mediated by both the (damping) radiative feedback and the (damping, diffusive) dynamic AHT feedback.

The weaker sensitivity of temperature to spatial patterns of D when AHT can adjust (relative to fixed AHT) is also clearly seen in the climate impact of synthetic patterns of D (Fig. 3f). For example, the strengthening of the equator-to-pole temperature gradient when setting $D(x)=\overline{D}/2$ is larger in magnitude under fixed AHT as compared to that in the full MEBM (cf. the dashed blue line in 2f versus 3f) because in the former case the temperature gradient has to steepen in order to restore the (prescribed) AHT while in the latter case allowing poleward AHT to decrease (Fig. 3h) requires less steepening of the temperature gradient.

The climatological pattern of $E-P$ in the full MEBM is smoother than its prescribed AHT counterpart (cf. Figures 2c and 3c). Specifically, the bimodal tropical precipitation predicted in the prescribed AHT is related to the kink in the AHT curve near the equator (Fig. 2d) which is absent in the full MEBM (Fig. 3d) due to the limitations of the purely linear T-dependence of the OLR parameterization in the region of deep convective clouds within the intertropical convergence zone. Similar to the finding above, the climatological pattern of $E-P$ is less sensitive to spatial anomalies in D in the full MEBM setting as compared to the fixed AHT setting (cf. Figure 2g, 3g), which we understand as follows: under fixed AHT, latent heat fluxes and, thus, $E-P$ can only change if the moist/dry partitioning changes; and that is dictated by local temperature changes via the Clausius-Clapeyron relation in the MEBM. The same local thermodynamic control on $E-P$ is present in the full MEBM, but this sensitivity is generally countered in the tropics by the impact of total AHT changes. For example, for $D(x)=\overline{D}/2$, the tropics warm—favoring an enhancement of moisture input and precipitation to the deep tropics as seen in the fixed AHT setting (Fig. 2g)—but the reduced diffusion weakens the magnitude of total AHT thereby reducing the magnitude of the hydrologic cycle.

Overall, the climatological MEBM is relatively insensitive to the spatial structure of diffusivity because the impact of spatial anomalies in diffusivity can be counterbalanced by modest temperature adjustments that are further damped by radiative feedbacks in the full dynamical system.

3 The impact of diffusivity on the perturbation climate response

We next evaluate how the spatial pattern of D affects the perturbation climate response to climate forcing. Following Siler et al. (2018), we consider a perturbation version of the MEBM. Let $R_f(x)$ be the perturbation in the radiative forcing at the top of the atmosphere, $G(x)$ be the change in net surface heat fluxes associated with ocean heat uptake, $\lambda(x)$ be the local net radiative feedback, $T'(x)$ be the perturbation near-surface temperature; and $F'(x)$ be the change in AHT. Conservation of energy then gives

$$R_f(x) = G(x) - \lambda(x)T'(x) + \frac{1}{2\pi a^2}\frac{d}{dx}F'(x) \tag{4}$$

where

$$F'(x) = -\frac{2\pi p_s}{g}D(x)\left(1-x^2\right)\frac{dh'}{dx} \tag{5}$$

Siler et al. (2018) diagnosed $R_f(x)$, $G(x)$, and $\lambda(x)$ from an ensemble of CMIP5 models for a CO_2 quadrupling

experiment (which we show below). Using a constant and uniform value of D, Siler et al. (2018) showed that the perturbation MEBM (Eqs. (4) and (5)) gave solutions for T', F', and $E' - P'$ in good agreement with the CMIP5 models. We here evaluate how the Siler et al. (2018) results change for different spatial patterns of diffusivity.

Figure 4a shows the spatial pattern of diffusivity D_{CMIP5} diagnosed from the ensemble mean of the $4 \times CO_2$ runs, and a reference, uniform, diffusivity D_0 is chosen so that $T_{4\times CO_2}(x)$ calculated by the MEBM gives the best agreement with CMIP5. Figures 4b–d show MEBM solutions for T', F', and $E' - P'$, calculated with the two spatial patterns of diffusivity, and compared to the ensemble-mean CMIP5 results. For the MEBM calculations, it is clear that the spatial pattern of diffusivity makes only a small difference to the solutions. AHT is particularly invariant to variations in $D(x)$ (Fig. 4d) as it is governed by energy fluxes (Armour et al. 2019). Using a spatially varying $D(x) = D_{CMIP5}$ with enhanced diffusivity in mid-latitudes leads to slightly warmer high-latitude temperatures than constant D, but the magnitude is less than 1 °C everywhere, and so much less than model-to-model differences among the CMIP5 results, or typical uncertainties associated with different emissions scenarios. This is consistent with Siler et al. (2018) and Bonan et al. (2018, 2023) who showed that the MEBM emulated the spatial patterns of T', and $E' - P'$ in individual GCMs within the CMIP5 ensemble using a single constant value for D for all calculations.

In the second row of Fig. 4, we evaluate the impact of the same synthetic patterns for $D(x)$ from Fig. 2, where the patterns are added as perturbations to the standard MEBM case (the solid black lines in the top row of Fig. 4). Results in Figs. 4f–h are presented as differences from the standard case. In general, the compensating nature of the MEBM response to changing diffusivity keeps the changes small. For example, setting $D(x) = \overline{D}/2$, the temperature gradient increases, but there is also a decrease in F' offsetting this. Of note, we find that the pattern of changes in T' is not symmetric with respect to the equator, and are larger in the southern hemisphere. This is caused by changes of F', which mainly happen in the southern hemisphere (Fig. 4d, h), in response to high-latitude ocean heat uptake there (Siler et al. 2018; Armour et al. 2019).

4 The relative importance of the spatial pattern of diffusivity

Finally, we evaluate the importance of the spatial pattern of $D(x)$ relative to the spatial patterns of the other inputs to the perturbation version of the MEBM, $R_f(x)$, $G(x)$, and $\lambda(x)$, on the spatial pattern of climate reponse. An earlier related study, Rencurrel and Rose (2018) used an energy-balance approach to argue that it is the spatial pattern of cloud forcing that is most important for setting the climate response to patterns of ocean-heat transport. For ease of presentation, we combine the spatial structure of radiative forcing $F(x)$ and ocean heat uptake $G(x)$ in Eq. 4 into a single variable $R(x) = R_f(x) + G(x)$, which represents the prescribed anomaly in energy flux at each latitude. Figure 5a shows the CMIP5 ensemble-mean patterns of $R(x)$, $\lambda(x)$ and $D_{4\times CO_2}(x)$, together with their global means. In Fig. 5b, c we show the impact of the spatial structure of each of $R(x)$, $\lambda(x)$ and $D_{4\times CO_2}(x)$ on T' and $E' - P'$, which is calculated by replacing the spatially varying profiles of each parameter with globally uniform (equal to global-mean) values in the

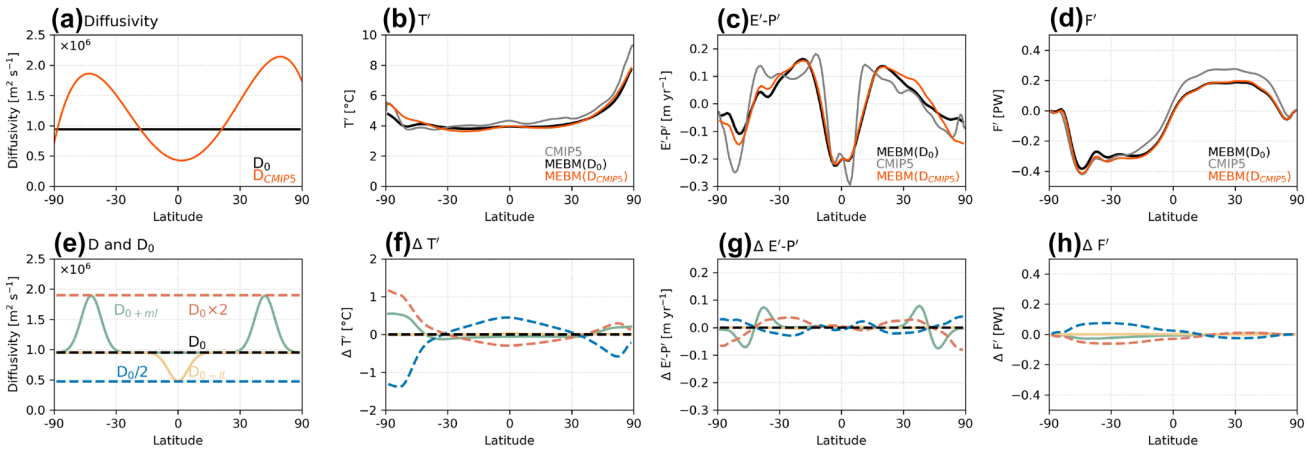

Fig. 4 Effects of different patterns of diffusivity, $D(x)$, on the climate change in the perturbation MEBM. First row: the impact of spatially-varying versus spatially-uniform diffusivity: (**a**) $D(x)$ diagnosed from CMIP5 (red line) and D_0 (black line); (**b**) T', (**c**) $E' - P'$, and (**d**) $F'(x)$ in CMIP5 outputs (grey line) and calculated from perturbation MEBM (Eqs. 4 and 5) based on input of $D(x)$ in (a). Second row: the impact of varying the magnitude or pattern of diffusivity: (**e**) synthetic patterns of $D(x)$; (**f**) T'; (**g**) $E' - P'$; and (h) $F'(x)$ derived from perturbation MEBM based on using different input of $D(x)$ from (e)

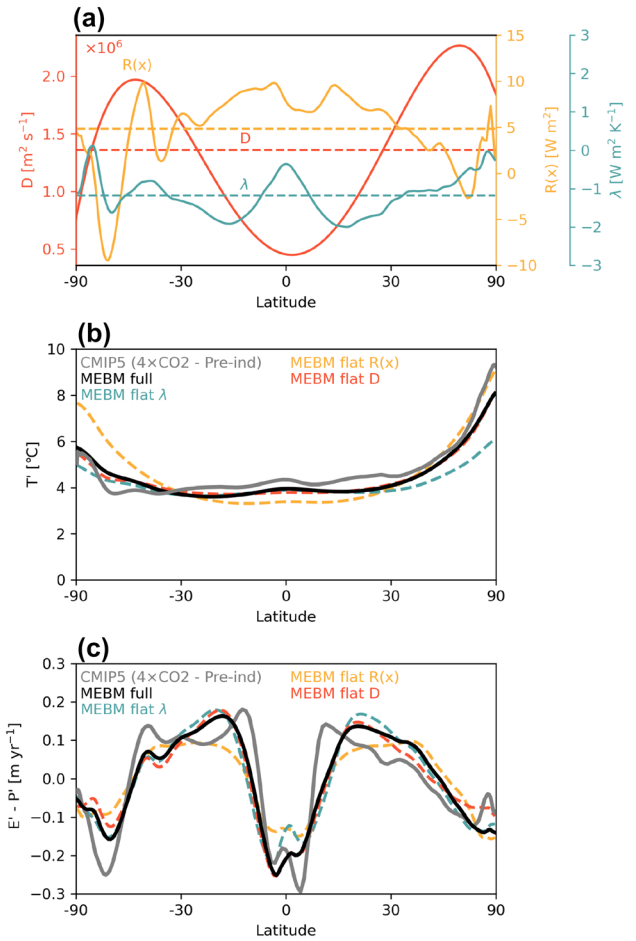

Fig. 5 **a** Spatial patterns of feedback $\lambda(x)$, anomaly energy flux at each latitude $R(x) = R_f(x) + G(x)$, and diffusivity $D(x)$ diagnosed from CMIP5 ensemble-mean output. Flat lines show the global-mean values of each. **b** T' from the perturbation MEBM for various experiments by setting one of three inputs from (**a**) as spatially-uniform while keeping the other two inputs spatially varying. **c** as for (**b**) but showing $E' - P'$

MEBM while keeping the other two parameters set to their spatially varying values. The difference between the solutions to the MEBM with the full spatial structure of forcing, feedback and D (black line in Fig. 4) and the solutions with flattened forcing (orange), feedbacks (blue) and diffusivity (red) can be thought of as how much the spatial structure in that parameter contributes to the spatial structure of temperature and hydrological change. Also shown are the CMIP5 ensemble-mean changes under $4 \times CO_2$ (gray line).

When $\lambda(x)$ is replaced with its global-mean value, the biggest impact on T' is in the high northern latitudes where the more-positive values of the feedback contribute to polar amplification (blue lines, Fig. 5b, c). Changes elsewhere are small (< 0.3 ℃), even though Bonan et al. (2018, 2023) determined that variation of $\lambda(x)$ was the leading cause of intermodel variations in T' and $E' - P'$ among CMIP5 models. Replacing $R(x)$ with its global-mean value (orange lines, Fig. 5b,c) has the biggest impacts at high southern latitudes, due to the importance of Southern Ocean heat uptake reducing the polar amplification. The slight tropical cooling again reflects the weaker T' gradients associated with reduced F' into the southern hemisphere. Finally, of least importance is the spatial pattern of $D(x)$ (red lines, Fig. 5b,c), which causes changes in T' of less than 0.2 ℃ everywhere. The small impact of the spatial pattern of D explains why, in previous research, the MEBM was able to successfully emulate the climate response with a single, constant, and uniform value of D for all models (Siler et al. 2018; Armour et al. 2019; Bonan et al. 2018, 2023).

The analyses in this section demonstrate the power of downgradient transport to produce smooth patterns of climate response even in the face of strong spatial variations in input forcing fields. We also direct readers to Bonan et al., (2018, 2023) who evaluate how the differences in the spatial patterns of input fields diagnosed from individual GCMs affects the patterns and amplitudes of the temperature and hydrologic climate responses. Their analyses are consistent with our findings here.

5 Conclusions

The principal that the atmospheric circulation acts to provide a downgradient transport of moist static energy is useful for understanding how atmospheric heat transport orchestrates the temperature and hydrologic response to climate change; and how it ties together regional variations in climate forcing, top-of-atmosphere radiative damping, and ocean heat uptake. In this study, we have relaxed an assumption made in much prior work that AHT is governed by downgradient transport with a globally uniform efficiency, or diffusivity.

Diagnosing the spatial pattern of the diffusivity from Eq. (3) using an atmospheric reanalysis, we found that the observed diffusivity varies approximately two-fold seasonally and three-fold spatially, with the highest values in the wintertime mid-latitudes. For reasons that are not clear, we found that the diffusivity varies more with latitude in GCM ensembles than in observations. We also find that the magnitude and spatial pattern of diffusivity in GCMs remains remarkably similar in simulations of the pre-industrial climate, a climate with CO_2 levels four times higher, and at the LGM, suggesting that the efficiency of the atmospheric heat transport is not especially sensitive to changes in the mean state or to changes in surface boundary conditions such as the presence of continental-scale ice sheets or the absence of year-round sea ice.

A motivating question for this study was, given these substantial spatial and seasonal variations in D, why do MEBMs with spatially uniform values of D capture the

basic structure of temperature and hydrologic changes under forcing simulated by comprehensive climate models? The temperature adjustment needed to maintain a given AHT when changing from a spatially uniform D to the observationally-derived spatial pattern of D is modest (Fig. 2b) because small changes in the temperature gradient can provide the changes in MSE gradient needed to counterbalance the impact of D anomalies on AHT. The climate simulated by the full MEBM (Fig. 3) is even less sensitive to the spatial pattern of diffusivity because the temperature response to spatial anomalies in D are damped by the sum of the AHT and radiative response. Stated otherwise, in the full MEBM the energetic tendencies depend on the curvature of h with only modest changes need to counter-balance local bumps in D. The role of moisture is significant – it explains why the biggest impacts on T are in the middle- and high- latitudes, where T forms a bigger part of h. These same conclusions hold for the perturbation model where the spatial pattern in diffusivity only impacts the local curvature of temperature and makes a smaller impact on regional climate than either the spatial patterns of climate forcing or radiative damping.

Our results help to explain why previous research that used a single, constant value for diffusivity in an MEBM successfully emulated the spatial patterns of climate change within GCMs. Our interpretation here is that the basic diffusive nature of downgradient transport means that the detailed pattern of its efficiency does not matter for capturing the basic structure of the zonal-mean temperature response. Compared to a dry EBM, the inclusion of both latent heat and sensible heat in the MEBM strengthens the insensitivity to $D(x)$, because the same change in energy gradient is accomplished by a smaller change in T' . Thus, an outcome of our analyses is that downgradient transport can be used as a useful conceptual framework for understanding climate and climate change, or for comparing different GCM simulations, without having to do a detailed calibration of $D(x)$ in each case.

Equation (1) is the simplest representation of physical tendency for downgradient transport. Further work might evaluate whether observations exhibit a different diffusivity for sensible and latent heat (e.g., Lu et al. 2022), or consider higher-order (nonlinear) dependencies on the gradient. Improved fits are surely possible, at the expense of extra parameters. However, our results suggest that it is the principle of downgradient transport that is more important for understanding the fundamental structure of zonal-mean climate change than its detailed functional form.

Appendix A

See Appendix Table 1.

We follow Siler et al. (2018) in implementing a hydrologic cycle within the MEBM. We specify a Gaussian weighting function, $w(x)$, to separate the total heat transport into eddy ($F_{\text{eddy}}(x)$) and Hadley Cell ($F_{\text{HC}}(x)$) components:

$$F_{\text{eddy}}(x) = [1 - w(x)]F(x) \tag{A1}$$

$$F_{\text{HC}}(x) = w(x)F(x) \tag{A2}$$

We set $w(x) = \exp[-(x/\sigma_x)^2]$, where $\sigma_x = \sin(15°) \approx 0.26$, so that $F_{\text{eddy}}(x)$ accounts for nearly all energy transport in mid-to-high latitudes, while $F_{\text{HC}}(x)$ accounts for most energy transport in low latitudes within 15°. $F_{\text{HC}}(x)$ is quantified by

$$F_{\text{HC}}(x) = \psi(x)g(x) \tag{A3}$$

where $\psi(x)$ is the Hadley Cell mass transport (with southward transport in the lower branch equal to northward transport in the upper branch,) and $g(x)$ is the gross moist stability of the atmosphere, defined as the difference between MSE in the upper and lower branches at each latitude. Following Held (2001), we assume that MSE is uniform ($\equiv h_u$), throughout the upper branch of the Hadley cell such that variations in $g(x)$ are primarily caused by meridional

Table 1 CMIP5 models used in this study

Model	$4\times CO_2$	Pre-Industrial	LGM	R_f ($4\times CO_2$)	G ($4\times CO_2$)	λ ($4\times CO_2$)
BCC CSM1-1	×	×		×	×	×
CAN ESM2	×	×		×	×	×
CCSM4	×	×	×	×	×	×
CSIRO MK3	×	×		×	×	×
FGOALS S2	×	×		×	×	×
GFDL CM3	×	×		×	×	×
INMCM4	×	×		×	×	×
MIROC5	×	×		×	×	×
MRI-CGCM3	×	×	×	×	×	×
NORESM1-M	×	×		×	×	×

The PI and LGM climatologies are calculated from the last 50 years of the simulation. Climatologies for the $4\times CO_2$ simulations are calculated using years 50–100 after quadrupling

variations in near-surface MSE: $g(x) = h_u - h(x)$, where we set $h_u = 1.07h(x = 0)$, or 7% above the near-surface MSE at the equator, which is a reasonable approximation to the observed profile (Siler et al. 2018). We can get $g(x)$ from the MEBM output fields, and hence solve for $\psi(x)$ from (A2) and (A3). Finally, assuming the upper branch of the Hadley Cell is dry, moist heat transport ($F_{\mathrm{HC},q}$) is confined in the lower branch, implying that

$$F_{\mathrm{HC},q}(x) = -\psi(x)Lq(x) \tag{A4}$$

Finally, we derive $E - P$ by taking the divergence of $F_{eddy,q} + F_{\mathrm{HC},q}$.

Acknowledgements We thank the editor Jian Lu, and three reviewers.

Author contribution All authors contributed to the design, analyses, and writing of the manuscript.

Funding Q.G., A.D., K.C.A., and G.H.R were supported by National Science Foundation Award CLD2019647.

Data availability The ERA5 data used in this study are available at https://cds.climate.copernicus.eu/cdsapp#!/dataset/reanalysis-era5-pressure-levels. The CMIP5 data used in this study are available at https://esgf-node.llnl.gov/search/cmip5/.

Declarations

Conflict of interest The authors have no relevant financial or non-financial interests to disclose.

References

Armour KC, Siler N, Donohoe A, Roe GH (2019) Meridional atmospheric heat transport constrained by energetics and mediated by large-scale diffusion. J Clim 32(12):3655–3680. https://doi.org/10.1175/JCLI-D-18-0563.1

Barry L, Craig GC, Thuburn J (2002) Poleward heat transport by the atmospheric heat engine. Nature 415(6873):774–777. https://doi.org/10.1038/415774a

Bonan DB, Armour KC, Roe GH, Siler N, Feldl N (2018) Sources of uncertainty in the meridional pattern of climate change. Geophys Res Lett 45(17):9131–9140. https://doi.org/10.1029/2018GL079429

Bonan DB, Siler N, Roe GH, Armour KC (2023) Energetic constraints on the pattern of changes to the hydrological cycle under global warming. J Clim 36(10):3499–3522. https://doi.org/10.1175/JCLI-D-22-0337.1

Braconnot et al, Evaluation of climate models using palaeoclimatic data (2012) Nat Clim Change 2, 417–424. https://doi.org/10.1038/nclimate1456

Chang CY, Held IM (2022) A scaling theory for the diffusivity of poleward eddy heat transport based on Rhines scaling and the global entropy budget. J Atmos Sci 79(6):1743–1758. https://doi.org/10.1175/JAS-D-21-0242.1

Cox T, Donohoe A, Roe GH, Armour KC, Frierson DM (2022) Near invariance of poleward atmospheric heat transport in response to midlatitude orography. J Clim 35(13):4099–4113. https://doi.org/10.1175/JCLI-D-21-0888.1

Donohoe A, Armour KC, Roe GH, Battisti DS, Hahn L (2020) The partitioning of meridional heat transport from the Last Glacial Maximum to CO_2 quadrupling in coupled climate models. J Clim 33(10):4141–4165. https://doi.org/10.1175/JCLI-D-19-0797.1

Feldl N, Roe GH (2013) The nonlinear and nonlocal nature of climate feedbacks. J Clim 26(21):8289–8304. https://doi.org/10.1175/JCLI-D-12-00631.1

Flannery BP (1984) Energy balance models incorporating transport of thermal and latent energy. J Atmosp Sci 41(3):414–421. https://doi.org/10.1175/1520-0469(1984)041%3c0414:EBMITO%3e2.0.CO;2

Held IM (2001) The partitioning of the poleward energy transport between the tropical ocean and atmosphere. J Atmos Sci 58(8):943–948. https://doi.org/10.1175/1520-0469(2001)058%3c0943:TPOTPE%3e2.0.CO;2

Hersbach, H, Bell, B, Berrisford, P, Hirahara, S, Horányi, A, Muñoz-Sabater, J., ... Thépaut, JN (2020) The ERA5 global reanalysis. Q J R Meteorol Soc 146(730): 1999–2049. https://doi.org/10.1002/qj.3803

Hwang, YT, Frierson, DM (2010) Increasing atmospheric poleward energy transport with global warming. Geophys Res Lett 37(24). https://doi.org/10.1029/2010GL045440

Hwang, YT, Frierson, DM, Kay, JE (2011) Coupling between Arctic feedbacks and changes in poleward energy transport. Geophys Res Lett 38(17). https://doi.org/10.1029/2011GL048546

Lapeyre G, Held IM (2004) The role of moisture in the dynamics and energetics of turbulent baroclinic eddies. J Atmos Sci 61(14):1693–1710. https://doi.org/10.1175/1520-0469(2004)061%3c1693:TROMIT%3e2.0.CO;2

Lu J, Zhou W, Kong H, Leung LR, Harrop B, Song F (2022) On the diffusivity of moist static energy and implications for the polar amplification response to climate warming. J Clim 35(21):7127–7146. https://doi.org/10.1175/JCLI-D-21-0721.1

Merlis TM, Henry M (2018) Simple estimates of polar amplification in moist diffusive energy balance models. J Clim 31(15):5811–5824. https://doi.org/10.1175/JCLI-D-17-0578.1

Merlis TM, Feldl N, Caballero R (2022) Changes in poleward atmospheric energy transport over a wide range of climates: energetic and diffusive perspectives and a priori theories. J Clim 35(20):6533–6548. https://doi.org/10.1175/JCLI-D-21-0682.1

Mooring, TA, Shaw, TA (2020) Atmospheric diffusivity: a new energetic framework for understanding the midlatitude circulation response to climate change. Journal of Geophysical Research: Atmospheres, 125(1). https://doi.org/10.1029/2019JD031206

North GR (1975) Theory of energy-balance climate models. J Atmosp Sci 32(11):2033–2043. https://doi.org/10.1175/1520-0469(1975)032%3c2033:TOEBCM%3e2.0.CO;2

Pierrehumbert RT (2010) Principles of planetary climate. Cambridge University Press, Cambridge, UK

Rencurrel, MC, & Rose, BE (2018). Exploring the climatic response to wide variations in ocean heat transport on an aquaplanet. J Clim 31(16): 6299–6318. /https://doi.org/10.1175/JCLI-D-17-0856.1

Roe GH, Feldl N, Armour KC, Hwang YT, Frierson DM (2015) The remote impacts of climate feedbacks on regional climate predictability. Nat Geosci 8(2):135–139. https://doi.org/10.1038/ngeo2346

Rose BE, Armour KC, Battisti DS, Feldl N, Koll DD (2014) The dependence of transient climate sensitivity and radiative feedbacks on the spatial pattern of ocean heat uptake. Geophys Res Lett 41(3):1071–1078. https://doi.org/10.1002/2013GL058955

Shaw TA, Voigt A (2016) What can moist thermodynamics tell us about circulation shifts in response to uniform warming? Geophys Res Lett 43(9):4566–4575. https://doi.org/10.1002/2016GL068712

Siler N, Roe GH, Armour KC (2018) Insights into the zonal-mean response of the hydrologic cycle to global warming from a

diffusive energy balance model. J Clim 31(18):7481–7493. https://doi.org/10.1175/JCLI-D-18-0081.1

Taylor K, Stouffer R, Meehl G (2012) An overview of CMIP5 and the experiment design. Bull Am Meteorol Soc 93:485–498. https://doi.org/10.1175/BAMS-D-11-00094.1

Trenberth KE, Caron JM (2001) Estimates of meridional atmosphere and ocean heat transports. J Clim 14(16):3433–3443. https://doi.org/10.1175/1520-0442(2001)014%3c3433:EOMAAO%3e2.0.CO;2

Publisher's Note Springer Nature remains neutral with regard to jurisdictional claims in published maps and institutional affiliations.

Springer Nature or its licensor (e.g. a society or other partner) holds exclusive rights to this article under a publishing agreement with the author(s) or other rightsholder(s); author self-archiving of the accepted manuscript version of this article is solely governed by the terms of such publishing agreement and applicable law.